Three Worlds in One: Venus as a Natural Laboratory for the Effect of Rotation Period on Atmospheric Circulation

Maureen Cohen, James Holmes, Stephen Lewis, Manish Patel, Sébastien Lebonnois

The Astrophysical Journal Letters, 980:L11 (10pp), 2025 February 10 https://doi.org/10.3847/2041-8213/adade9

Three Worlds in One: Venus as a Natural Laboratory for the Effect of Rotation Period on Atmospheric Circulation

Maureen Cohen[1], James Holmes[1], Stephen Lewis[1], Manish Patel[1], and Sébastien Lebonnois[2]
[1] School of Physical Sciences, The Open University, Milton Keynes, MK7 6AA, UK
[2] Laboratoire de Météorologie Dynamique (LMD/IPSL), Sorbonne Université, ENS, PSL Research University, Institut Polytechnique de Paris, CNRS, Paris, France
Received 2024 November 11; revised 2025 January 17; accepted 2025 January 17; published 2025 February 6

Abstract

Because of its rotation period of 243 days, Venus is considered a slowly rotating planet. However, its persistent superrotating atmospheric jets, which increase in speed from surface to cloud tops, effectively set a faster rotation speed than the surface rotation. Using the Venus Planetary Climate Model and wind measurements taken by the Pioneer Venus entry probes, we show that the Rossby radius of deformation of the atmosphere varies with height. The atmosphere falls into three circulation regimes: (1) from the surface to 20 km, the Rossby radius of deformation exceeds the planetary radius and no Rossby waves form; (2) from 20 to 50 km, the tropical Rossby radius becomes smaller than the planetary radius, and a circulation regime characterized by a superrotating equatorial jet and mid-latitude Rossby gyres appears; (3) from 50 to 70 km, the extratropical Rossby radius becomes smaller than the planetary radius, the jet develops mid-latitude maxima, and the Rossby gyres shift to high latitudes. Studies of exoplanetary circulation regimes as a function of rotation period have repeatedly shown a similar progression. While observing the circulations of exoplanets to confirm these predictions is not currently possible, the presence of different circulation regimes on Venus and their dependence on altitude could be tested by observing campaigns. Such evidence would be the first observational support for the theory connecting differences in planetary rotation periods to circulation regime transitions and would ground predictions of exoplanet circulations in a validated framework.

Unified Astronomy Thesaurus concepts: Venus (1763); Atmospheric dynamics (2300); Planetary atmospheres (1244); Exoplanet atmospheres (487)

Materials only available in the online version of record: animations

1. Introduction

With a period of 243 Earth days, Venus is the slowest rotating planet in the solar system. The planet's sluggish rotation at the surface contrasts with its dynamic cloud decks between 45 and 70 km, where superrotating jets reach speeds high enough for the atmosphere to circle the planet once every 5 days (C. C. Counselman et al. 1979, 1980; A. Seiff et al. 1980, 1985; M. Newman et al. 1984). Extensive literature on the atmospheric dynamics of Venus has sought to explain its cloud-level superrotation in terms of the "Gierasch–Rossow–Williams" mechanism, in which a thermally direct Hadley-like circulation transports angular momentum upwards and polewards from the equator to drive two mid-latitude jets, from which nonaxisymmetric eddies, in turn, pump the angular momentum upgradient back toward the equator (P. J. Gierasch 1975; W. B. Rossow & G. P. Williams 1979; M. Yamamoto & M. Takahashi 2003; C. Lee et al. 2007; S. Lebonnois et al. 2010, 2016; N. Sugimoto et al. 2014a, 2014b; M. Takagi et al. 2018, 2023; T. Imamura et al. 2020; A. Suzuki et al. 2022). While the modeling and theory of Venus' atmospheric dynamics have remained challenging, observational evidence in the form of direct meridional wind measurements, trace gas species distributions, and cloud imaging supports the existence of a cloud deck-level Hadley cell and mid-latitude eddies (C. C. Counselman et al. 1980; A. D. Collard et al. 1993; E. Marcq et al. 2005, 2006; T. Horinouchi et al. 2023). Studies of the deep atmosphere, however, have suggested other mechanisms driving the winds here: M. Yamamoto & M. Takahashi (2004) and M. Yamamoto & M. Takahashi (2006) proposed that superrotation in the Venus deep atmosphere is instead caused by a coupled equatorial Kelvin wave and high-latitude Rossby wave driving angular momentum toward the equator.

The discovery of thousands of exoplanets has prompted a surge of new interest in the potential atmospheric circulations of planets rotating with periods different from that of Earth (A. Showman et al. 2010; J. Leconte et al. 2013; A. P. Showman et al. 2013; N. J. Mayne et al. 2014; T. D. Komacek & D. S. Abbot 2019; X. Tan & T. D. Komacek 2019; F. Debras et al. 2020). Due to the observational biases of most exoplanet detection methods, many of the known exoplanets are in close-in orbits, tidally locked, and—like Venus—rotating with periods longer than 1 Earth day (R. Barnes 2017; L. D. Deming & S. Seager 2017). In simulations by 3D atmospheric models, the circulation of slowly rotating exoplanets typically also forms superrotating jets (A. P. Showman & L. M. Polvani 2011; S.-M. Tsai et al. 2014; M. Hammond & R. T. Pierrehumbert 2018; R. T. Pierrehumbert & M. Hammond 2019; M. Hammond et al. 2020; M. Hammond & N. T. Lewis 2021), falling into a progression of regimes dependent on planetary rotation period (T. M. Merlis & T. Schneider 2010; A. Edson et al. 2011; L. Carone et al. 2015; S. Noda et al. 2017; J. Penn & G. K. Vallis 2018; E. Landgren et al. 2023). Whether these circulation regimes appear on real worlds is not easy to determine given the difficulty of retrieving details of exoplanet

atmospheres, though some work has provided observational support for superrotation (H. A. Knutson et al. 2008; D. J. Armstrong et al. 2016; A. P. Asnodkar et al. 2022). Nevertheless, theories from the recent work on slow rotators outside the solar system can open up new avenues for understanding the atmospheric dynamics of Venus, while observations of Venus can shed light on how the circulation of a slowly rotating planet actually develops.

In the present study, we bring together two strands of scholarship by expanding an exoplanet climate dynamics framework developed by A. Edson et al. (2011) and L. Carone et al. (2015) and applying it to simulations by a state-of-the-art, validated Venus global climate model (S. Lebonnois et al. 2010). We show that the simulated circulations of the Venus deep atmosphere and of tidally locked exoplanets possess key features in common. In this framework, the increase in zonal wind speeds with altitude on Venus is equivalent to a change in the rotation period of the atmosphere (A. Sánchez-Lavega et al. 2017) and triggers transitions in circulation regime. This approach is compatible with observed and simulated features of the Venus atmosphere, opens up new theoretical approaches to understanding Venus's atmospheric dynamics, and is observationally testable. In Section 2 below, we describe our Venus climate model and the climate dynamics framework of L. Carone et al. (2015) for understanding planetary circulation regimes as a function of rotation period. In Section 3, we show that the simulated circulation of the Venus deep atmosphere resembles that of a tidally locked planet and that the circulation changes with altitude as a result of the changing effective rotation. In Section 4, we discuss how this framework is compatible with the existing literature on Venus's atmospheric dynamics, especially in regard to atmospheric waves. We conclude in Section 5.

2. Methods

2.1. Venus Planetary Climate Model Simulation

We simulate the Venus atmosphere using the Venus Planetary Climate Model (VPCM; S. Lebonnois et al. 2010; I. Garate-Lopez & S. Lebonnois 2018) of the Laboratoire Météorologie Dynamique. The VPCM consists of a longitude-latitude dynamical core (F. Hourdin et al. 2006) coupled to Venus-specific physics routines. The model is hydrostatic on hybrid sigma-pressure levels, and the kilometer altitudes for the pressure levels used in the figures below are based on the long-term mean geopotential height. The key physics routines are based on observational findings and include a specific heat adjustment with altitude according to the formula given in S. Lebonnois et al. (2010). The model incorporates a full radiative transfer scheme for the Venus atmosphere based on solar heating rates from R. Haus et al. (2015), an exchange rate matrix method from V. Eymet et al. (2009) for thermal radiation, and prescribed cloud and haze layers whose altitude decreases toward the poles (I. Garate-Lopez & S. Lebonnois 2018). It has surface topography derived from Magellan mission data and a boundary layer scheme described in F. Hourdin et al. (2002). The VPCM further includes an 11-layer soil model representing thermal conduction and a dry convective adjustment scheme (F. Hourdin et al. 1993; S. Lebonnois et al. 2010). We ran the model at a resolution of 96 latitudes by 96 longitudes, or 2° by 4°, and 50 vertical levels from the surface to 97 km, using the canonical planetary parameters for Venus stated in S. Lebonnois et al. (2010). The simulation was initialized from an already superrotating state and integrated for 94 Venus days, or approximately 30 Earth years. Atmospheric fields were averaged over this full period in the figures shown in Section 3, except where captions identify the figures as snapshots.

2.2. Climate Dynamics Framework

The atmospheres of slowly rotating planets experience competition between a thermally direct overturning circulation from the hot dayside to the cold nightside and the effects of rotation, which vary with rotation rate or period (J. L. Mitchell & G. K. Vallis 2010; A. P. Showman et al. 2013; R. T. Pierrehumbert & M. Hammond 2019). The atmospheric circulation falls into different equilibria—or circulation regimes—depending on the balance between these tendencies (R. T. Pierrehumbert & M. Hammond 2019). A key parameter in characterizing these circulation regimes is the Rossby radius of deformation, which defines the distance the fastest gravity waves can travel before feeling the effects of rotation (R. T. Pierrehumbert & M. Hammond 2019), as well as the maximum amplitude of planetary-scale Rossby waves. L. Carone et al. (2015) performed a large parameter space study of the atmospheric circulation of tidally locked terrestrial planets as a function of rotation period (1–100 Earth days) and described the resulting circulation regimes in terms of the tropical and extratropical meridional Rossby wavenumber. Expanding on A. Edson et al. (2011), L. Carone et al. (2015), and J. R. Holton & G. H. Hakim (2013), the tropical Rossby radius as a function of altitude z is

$$\lambda_R(z) = \sqrt{\frac{N(z)H(z)}{2\beta(z)}}, \tag{1}$$

where $N = \sqrt{\frac{g}{\theta(z)}\frac{d\theta}{dz}}$ is the Brunt–Väisälä (BV) frequency with g the gravitational constant and θ the potential temperature; $H = \frac{RT(z)}{\mu g}$ is the atmospheric scale height with R the gas constant, T the atmospheric temperature, and μ the mean molar mass of the atmosphere; and $\beta = \frac{2\Omega(z)}{R_p}$ in the equatorial beta plane approximation, with Ω the rotation rate and R_p the planetary radius. For the BV frequency, values below 40 km are set to the mean for this region to reduce noise; see Appendix A.1 for the effect of this choice on the calculation. The extratropical Rossby radius as a function of altitude is

$$L_R(z) = \frac{N(z)H(z)}{f(z)}, \tag{2}$$

where N and H are as above and $f = 2\Omega(z)\sin(v)$ is the Coriolis parameter with v representing latitude. Departing from L. Carone et al. (2015), we define all variables as a function of altitude in order to examine how circulation regime changes with height. We calculate $\Omega(z)$ as

$$\Omega(z) = \frac{\bar{u}(z)}{R_p + h(z)}, \tag{3}$$

where $\bar{u}(z)$ is the zonal and time mean (over 94 Venus days) of the zonal wind at a specific latitude, R_p is the planetary radius, and $h(z)$ is the altitude above the planetary surface. To arrive at the meridional Rossby wavenumber, we divide the tropical and

extratropical Rossby radii by the planetary radius R_p. All profiles calculated from the VPCM simulation use latitude-specific wind and temperature values to match the Pioneer Venus entry probes; see Appendix A.2 for a discussion of the sensitivity of the result to the choice of latitude.

L. Carone et al. (2015) show how the circulation regime changes when first the tropical, then the extratropical meridional Rossby wavenumber equal one. In conceptual terms, when the tropical Rossby radius of deformation equals the planetary radius, a tropical Rossby wave of zonal wavenumber 1 can "fit" on the planet. This correlates with a circulation regime characterized by a broad prograde superrotating equatorial jet and, for tidally locked planets, two large mid-latitude Rossby gyres associated with geopotential height anomalies confined to the nightside of the planet. When the extratropical Rossby radius of deformation equals the planetary radius, an extratropical (baroclinic) Rossby wave of zonal wavenumber 1 can fit on the planet. This corresponds to a circulation regime with two prograde mid-latitude jets associated with two smaller high-latitude Rossby gyres and geopotential height anomalies. When one or both meridional Rossby wavenumbers equal 0.5, L. Carone et al. (2015) find that either or both waves can be present and the circulation regime can fall into either of the described states or a mixture of them, indicating multistability. Below, we apply this framework to the Venus atmosphere to identify the altitudes that fall into these regimes.

3. Results

The VPCM simulation generates three different circulation regimes in three altitude regions: (1) the surface to 25 km, (2) 25–50 km, and (3) 50 km to the cloud tops at 70 km. Figure 1 shows a snapshot of the flow at one model level within each of these three regions, together with the eddy wind and eddy geopotential height (the deviation from the longitudinal mean, in each case). In the near-surface region in Figures 1(a) and (b), wind magnitudes are low, the eddy wind is disorganized, and the eddy geopotential height is a function of the underlying surface topography due to the hybrid vertical coordinate. In the 25–50 km region in Figures 1(c) and (d), a broad prograde equatorial superrotating jet forms, flanked by two large Rossby gyres centered at 75°W that extend from 50°N/S polewards. The eddy wind field clearly reveals the gyres and their associated positive and negative geopotential height anomalies. In simulations of tidally locked slowly rotating planets, these Rossby waves are described as stationary in the long-term mean, though some studies have found that their position oscillates (M. Cohen et al. 2023) or circumnavigates the globe (J. W. Skinner & J. Y.-K. Cho 2022; E. Landgren et al. 2023). In the VPCM simulation, the waves circumnavigate the planet on a timescale of 36 Earth days (M. Cohen et al. 2024). From 50 km up, Figures 1(e) and (f) reveal a widening superrotating jet with two maxima near 60°N/S. The circulation is complicated at and above the cloud tops by the superposition of solar thermal tides and a cloud-level Hadley cell. The Rossby gyres are not obvious in the wind field here as they become confined closer to the poles, but they remain visible in the eddy rotational component of the wind, extracted using a Helmholtz decomposition (J. Dutton 1976; A. Dawson 2016; M. Hammond & N. T. Lewis 2021) and displayed in Figure 1(f). These Rossby waves are in phase throughout the atmosphere and travel around the poles with the same periodicity.

We posit that the nature of the Rossby waves and the circulation regime change with height as the zonal wind speed, and therefore effective rotation speed of the atmosphere, increases from the surface upwards. While the solid body of the planet has a rotation period of 243 Earth days, the atmosphere "rotates" much more rapidly than this at the cloud-top level. The Venus atmosphere is therefore a natural laboratory for the effect of rotation rate on the circulation. Figure 2 shows the zonal wind speed and the effective rotation period of the atmosphere as a function of altitude for the VPCM simulation and the 1978 Pioneer Venus entry probes. Four entry probes (designated Day, Night, North, and Sounder) dropped by the Pioneer Venus space mission directly measured the thermal structure of the atmosphere from 126 to 12.4 km and the wind structure from 126 km to the surface; differential long baseline interferometry techniques applied to the radio signals received from the probes back on Earth made it possible to infer wind velocities (C. C. Counselman et al. 1979, 1980; A. Seiff et al. 1980). In both the model and probe data, the effective rotation period decreases from hundreds of days at 15 km to roughly 5 days in the upper cloud region. The VPCM simulation slightly underpredicts the measured wind values, but Figure 2 shows an otherwise good fit.

In Figure 3, we show the tropical and extratropical meridional Rossby wavenumbers for the VPCM simulation and the Pioneer Venus probes as a function of altitude. Where each profile crosses the dotted line, the Rossby radius of deformation equals the planetary radius, and we expect to see the circulation regime characterized by the tropical or extratropical Rossby wave appear. The tropical Rossby wavenumber equals unity at 20 km, where the Rossby gyres become visible in the flow, while the extratropical Rossby wavenumber hovers around unity from 40 to 50 km, in line with the shift of the Rossby gyres to polar latitudes. Because the VPCM underpredicts the wind speeds compared to the Pioneer Venus probes, the profiles calculated using the Pioneer Venus data locate the circulation regime transitions a few kilometers lower. In spite of these small differences, this analytical model correctly predicts the three vertical regions and their circulation regimes depicted in Figure 1.

Figure 4 depicts changes in structure over the vertical domain of the atmosphere related to the circulation regime change. Figure 4(a) shows a cross sectional snapshot of the deep atmosphere Rossby waves in the form of the eddy relative vorticity, a measure of the local rotation of the fluid, which is large within the Rossby gyres. The gyres appear between 20 and 30 km. They move poleward with height until they reach 75° at 50 km, after which their latitudinal position remains stable. Above 70 km, other strong sources of eddy relative vorticity become apparent; these travel at different speeds than the deep atmosphere Rossby gyres and are sometimes in phase and sometimes out of phase with them. Figure 4(b) traces the movement of the Rossby waves over time in the form of the temperature anomaly, or deviation of the air temperature from its long-term mean. The wave structure has an area of warmer air associated with upwelling at the leading edge of the gyre, such that a given coordinate experiences a periodic temperature fluctuation as the wave sweeps past. The plot shows the temperature anomaly of a single atmospheric column over 2 Venus solar days. From 20 to 50 km, a weak temperature

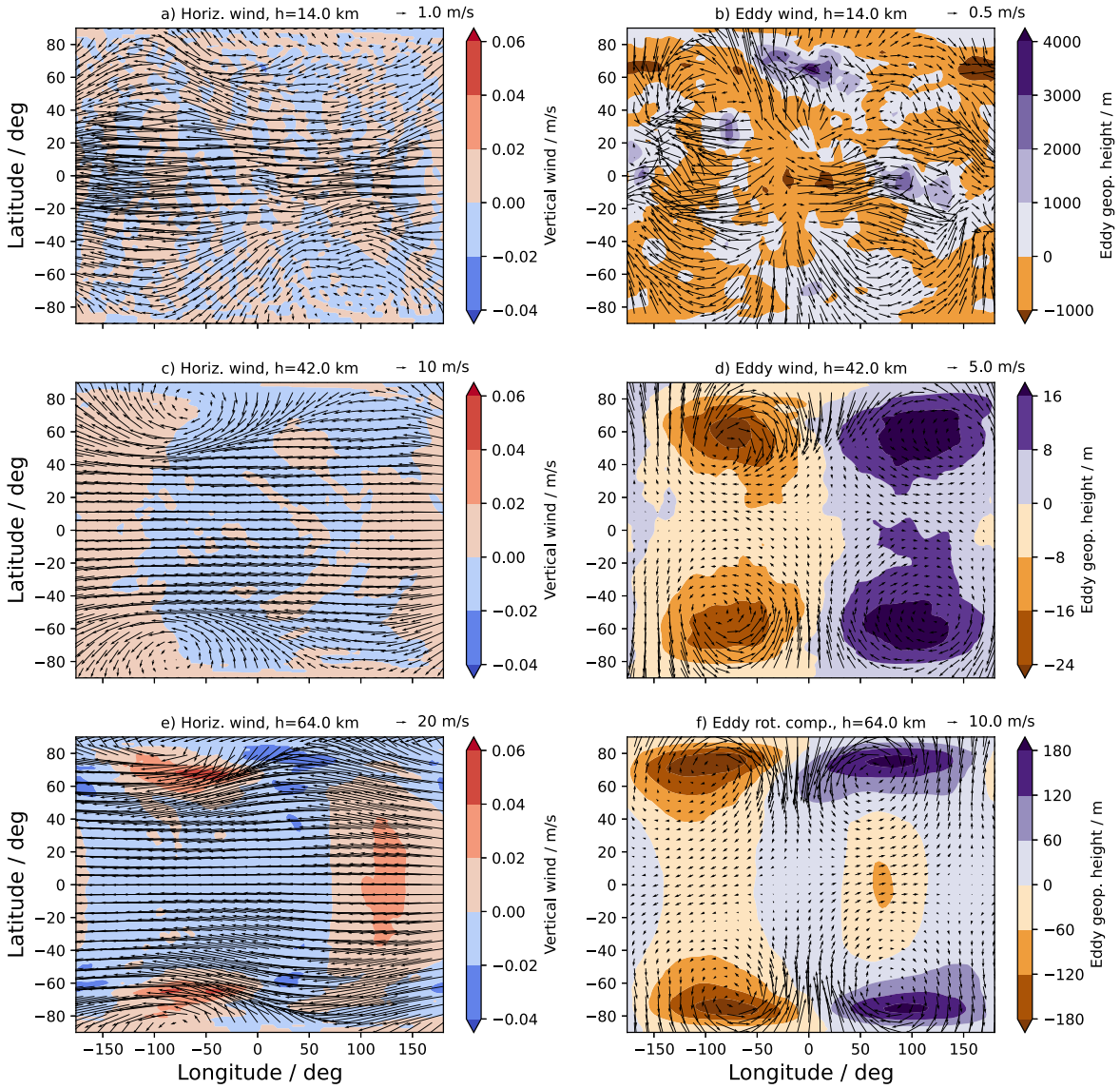

Figure 1. Left column: horizontal (quivers) and vertical (colors) wind at three different altitudes in the VPCM simulation. Right column: eddy winds and eddy geopotential height at the same three altitudes. In (b) and (d), the eddy wind is the wind field minus the zonal mean. In (f), the wind vectors shown are the eddy rotational component derived from a Helmholtz decomposition of the flow. All figures represent a snapshot taken at an identical simulation time with local noon at 135E. An animation of this figure over 3 Venus days, with 20 frames per Venus day, is available and further described in Appendix A.3. Note the quivers represent different wind magnitudes in each subfigure.

(An animation of this figure is available in the online article.)

fluctuation of 2 K associated with the Rossby waves is the only visible signal, with a periodicity of 36 Earth days. This fluctuation intensifies to 4–5 K above 50 km and a higher frequency signal begins to appear. From 60 to 70 km, where much of the solar energy is deposited into the upper cloud deck, a signal with the frequency of the Venus solar day appears, along with a high-frequency wave with a period of 4–5 Earth days. The superposition of these waves creates a more complex pattern and masks the weaker effect of the deep atmosphere Rossby waves.

4. Discussion

4.1. Compatibility with Existing Venus Literature

Using a simplified general circulation model, M. Yamamoto & M. Takahashi (2004) and M. Yamamoto & M. Takahashi (2006) describe a circulation pattern in the deep atmosphere in which a mid-latitude zonal wavenumber 1 Rossby wave and equatorial Kelvin wave jointly pump angular momentum toward the equator. This basic circulation pattern and super-rotation mechanism are the same as in our VPCM simulation and numerous simulations of slowly rotating, tidally locked exoplanets. These model predictions would be supported by the detection of a zonal wavenumber 1 Rossby wave in the relevant altitude range. Using Venus Express/VIRTIS-M data, C. C. C. Tsang et al. (2009) reported a time-varying abundance of carbon monoxide in the deep atmosphere polar latitudes, which, they argue, could be caused by a moving horizontal planetary wave feature, such as a Rossby wave. The trapping of carbon monoxide in globally traveling Rossby gyres could explain this variability and could be tested by a long-term observing campaign.

Considerably more attention has focused on the cloud deck altitude and above due to the greater availability of

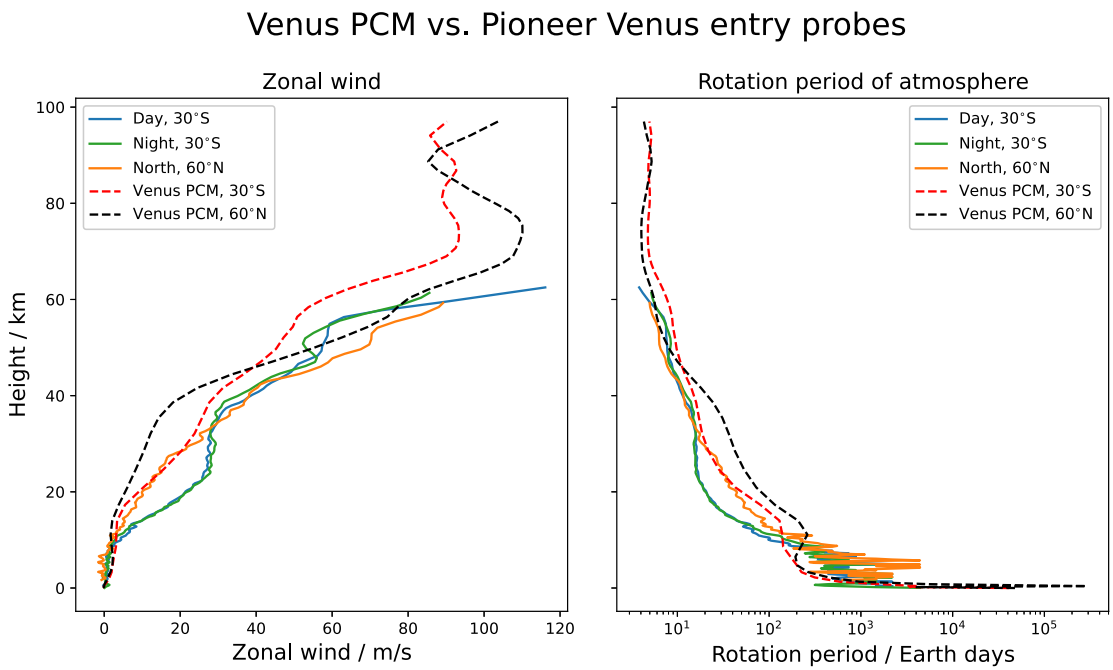

Figure 2. Left: vertical profiles of the zonal wind from the Venus PCM and three Pioneer Venus entry probes (Day, Night, and North). The Day and Night probes measured the wind profiles near 30°S, while the North probe entered near 60°N. The VPCM profiles are the zonal means at 30°S and 60°N. Right: the effective rotation period in Earth days of the atmosphere as a function of altitude for the VPCM simulation and the Day, Night, and North probes, calculated from the zonal wind profiles.

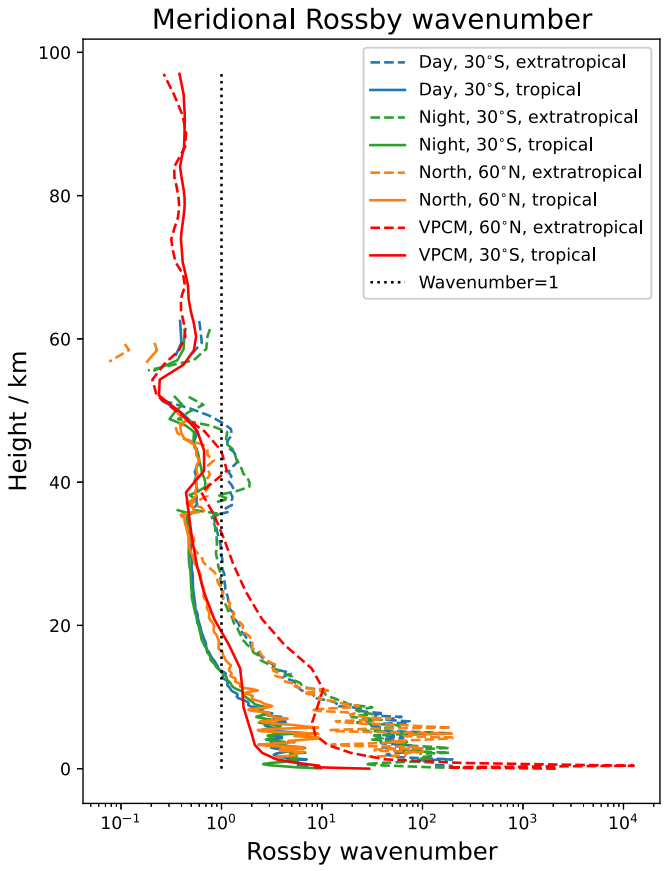

Figure 3. Tropical and extratropical meridional Rossby wavenumber as a function of altitude for the VPCM simulation and the Pioneer Venus Day, Night, and North entry probes. The dotted line indicates where the Rossby radius of deformation equals the planetary radius.

observations. Cloud imaging has repeatedly shown a Y-shaped feature, which may be caused by the superposition of cloud-level zonal wavenumber 1 mid-latitude Rossby and equatorial Kelvin waves moving with a 5 day period and a 4 day period, respectively (M. J. S. Belton et al. 1976; C. Covey & G. Schubert 1982; A. D. D. Genio & W. B. Rossow 1990; W. B. Rossow et al. 1990; T. Kouyama et al. 2012; I. V. Khatuntsev et al. 2013; M. Imai et al. 2016; H. Karyu et al. 2023). C. Covey & G. Schubert (1982) found that zonal wavenumber 1 waves of these types are resonant modes of the atmosphere. Numerical studies have indicated that the environment in the cloud decks, where most of the solar energy is deposited, is baroclinic (N. Sugimoto et al. 2014a), and that baroclinic waves can raise Rossby waves at the cloud tops (N. Sugimoto et al. 2014b). The transition to a baroclinic atmosphere in the cloud deck coincides with the shift to the extratropical (baroclinic) Rossby wave regime in our analysis. This past work is compatible with our framework's prediction that high-latitude baroclinic Rossby waves should be able to form at cloud-deck altitudes.

Figure 3 shows that from 50 km, both Rossby wavenumbers are similar and fall between 1 and 0.1. According to L. Carone et al. (2015), Rossby wavenumbers of ∼0.5 allow for multiple stable circulation regimes with either an equatorial jet and mid-latitude gyres or mid-latitude jets and high-latitude gyres, or a combination of both. Detailed work by M. Takagi et al. (2022), M. Takagi et al. (2023), D. Lai et al. (2024), and T. Horinouchi et al. (2020) describes, in simulations by two different models and observations by the Japanese Akatsuki Venus orbiter, how interaction between equatorial Kelvin and mid- and high-latitude Rossby waves alternately accelerates and decelerates the cloud-level equatorial superrotating jet on a timescale of 150 days. While these waves have shorter periods than the

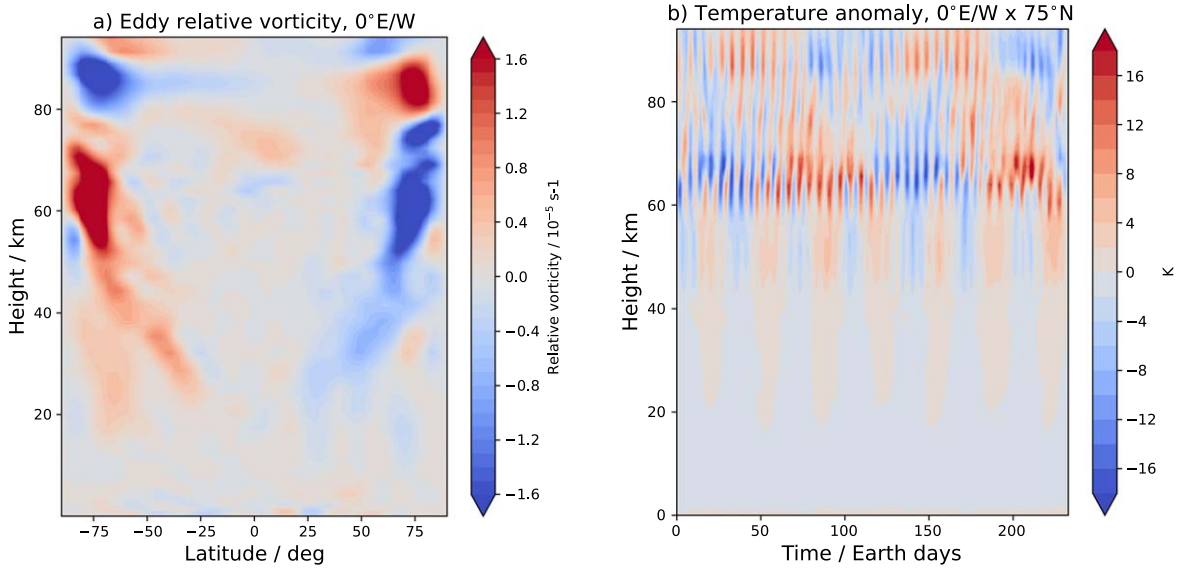

Figure 4. Left: altitude–latitude cross sectional snapshot of the eddy relative vorticity at longitude 0°. An animation of this subfigure over 3 Venus days, with 20 frames per Venus day, is available and further described in Appendix A.3. Right: altitude–time plot of the temperature anomaly at longitude 0° and latitude 75°N. (An animation of this figure is available in the online article.)

36 day wave in our study, the mechanism is compatible with a competition between the multiple possible circulation states expected for the altitude range where the Rossby wavenumbers are ∼0.5.

Finally, diurnal and semidiurnal solar tides also play a significant role in the cloud-level dynamics and angular momentum transport (R. A. Plumb 1975; A. Y. Hou & B. F. Farrell 1987; M. Takagi & Y. Matsuda 2007; M. Takagi et al. 2018; M. Yamamoto et al. 2024) and can take the form of tidal gyres (M. Yamamoto et al. 2024). S. Lebonnois et al. (2016) reported solar tides, barotropic, baroclinic, mixed Rossby-gravity, and Kelvin-type waves in an earlier study using the Venus PCM. Figure 4(b) reveals some of these waves in the temperature anomaly structure with periods of 1 Venus solar day and 4–5 Earth days; the amplitude of these waves is larger than that of the 36 day wave simulated in the deep atmosphere, and the long-period Rossby wave is no longer visible in the highly complex cloud deck environment. It is also possible that the long-period wave dissipates at or above the cloud deck. As these waves exist in the cloud decks and above, but not the deep atmosphere, it is not clear if the change in meridional Rossby wavenumber affects them as it does the 36 day wave in the VPCM simulation; however, observations could potentially determine whether, for example, solar tidal gyres have the characteristics (latitudinal position and association with jet structures) predicted by our framework in the altitudes between 40 and 70 km.

4.2. Implications for Venus and Exoplanet Research

Studies of exoplanet circulation patterns have found that certain rotation periods allow for multiple equilibrium climate states (A. Edson et al. 2011; L. Carone et al. 2015; D. E. Sergeev et al. 2022). D. E. Sergeev et al. (2022) showed that small differences in initial conditions could lead to either of the two circulation regimes described in Section 2.2 for an Earth-like planet rotating with a period of approximately 6 days, similar to the rotation speed of the Venus cloud-top atmosphere. If the Venus cloud-top circulation is in a state particularly sensitive to small changes in angular momentum transport, this could explain the apparent transience of the mid-latitude jet maxima, which are frequently simulated by models but only sometimes supported by observations (A. Sánchez-Lavega et al. 2017). If variability in the Venus cloud decks can be shown to be related to multistability in the circulation regime, this would support theoretical work on exoplanet atmospheric dynamics indicating that planets with similar rotation periods will have intrinsically less predictable circulations and climates (A. Hochman et al. 2022; D. E. Sergeev et al. 2022).

For exoplanet atmospheric dynamicists, it has proven difficult to validate model predictions with data, leading to a reliance on model intercomparisons (e.g., T. J. Fauchez et al. 2020; J. Haqq-Misra et al. 2022). Evidence supporting the existence of a deep atmosphere (C. C. C. Tsang et al. 2009; C. C. C. Tsang & K. McGouldrick 2017) or cloud-level (M. Imai et al. 2016; T. Horinouchi et al. 2020; M. Takagi et al. 2022; M. Yamamoto et al. 2023; D. Lai et al. 2024) Rossby–Kelvin wave coupling on Venus increases confidence in the ability of general circulation models to accurately simulate slow rotators. At the same time, the Venus atmosphere illustrates how such an idealized circulation regime framework can be complicated on a real planet by factors like cloud and haze formation or wave interactions.

5. Conclusion

In this study, we have shown that the simulated Venus atmosphere undergoes state changes in its circulation pattern that coincide with altitude thresholds where the Rossby radius of deformation for either tropical or extratropical Rossby waves equals the planetary radius. In the deepest section of the atmosphere below 20 km, no Rossby waves are present. From 20 to 50 km, the tropical Rossby radius becomes smaller than the planetary radius, and large mid-latitude Rossby gyres form, flanking an equatorial superrotating jet. From 50 km to the cloud tops, the extratropical Rossby radius becomes smaller than the planetary radius, and the Rossby gyres shrink and shift to the high latitudes, flanking two mid-latitude jet maxima.

These state changes occur because the effective rotation felt by the atmosphere increases with height due to the consistent increase in zonal wind profile, conditioning the environment to favor the formation of different types of rotational waves. Similar circulation patterns have been generated in many simulations of slowly rotating exoplanets, and evidence of their existence on Venus would support the validity of theoretical predictions by exoplanet general circulation models. While it is currently not feasible to observe the circulation of exoplanets to test theoretical predictions, characterizing the circulation on Venus as a function of altitude could be possible through observations of long-lived atmospheric tracer abundances. Venus could act as a "natural laboratory" for the effect of varying rotation period on the general circulation, grounding our theoretical understanding and motivating more confident predictions about the general population of planets inside and outside the solar system.

Acknowledgments

We are grateful to the UK Science and Technology Facilities Council for funding support through STFC grant ST/X001180/1. We also acknowledge and thank the NASA Space Science Data Coordinated Archive for maintaining and providing the data from the Pioneer Venus entry probes.

Data Availability

A subset of the Venus Planetary Climate Model simulation data used to create the visualizations in this study is available via doi:10.21954/ou.rd.c.7292911 under the names Surface and Cloud deck dataset. The Cloud deck dataset is used for Figure 4(b), while the Surface dataset is used for all other figures. The zonal wind, temperature, and pressure data returned by the Pioneer Venus entry probes is available on request from the NASA Space Science Data Coordinated Archive as part of the Pioneer Venus Special Events Data (SED) collection.

Software: We use the windspharm Python library (A. Dawson 2016) to perform the Helmholtz decomposition shown in Figure 1(f).

Appendix

A.1. Sensitivity to Brunt–Väisälä Frequency

We calculate the BV frequency according to the formula $N = \sqrt{\frac{g}{\theta(z)}\frac{d\theta}{dz}}$ and the potential temperature θ according to the formula given in S. Lebonnois et al. (2010) for an atmosphere in which specific heat capacity varies with altitude. Figure 5(a) shows the BV frequency calculated in this way for the Pioneer Venus temperature profiles and two comparable latitudes from the VPCM simulation. The Pioneer Venus profiles fluctuate rapidly below 40 km because the probes returned data only hundreds of meters apart and the conversion of temperature to potential temperature to BV frequency amplifies small differences between measurement points. The BV frequency also becomes imaginary in multiple places, leaving gaps in the profile. Similarly, the VPCM profile between 30 and 40 km disappears because the BV frequency becomes zero or imaginary in this region of negative or neutral stability. To smooth out these irregularities, we replace the values of the BV frequency below 40 km with the mean for this region, while retaining the calculated values above 40 km (Figure 5(b)). Figures 5(c) and (d) show the effect of this processing on the meridional Rossby wavenumber. The tropical Rossby radius clearly becomes unity at 20 km, where the tropical Rossby regime appears. However, in Figure 5(c) the extratropical Rossby radius is indeterminate between 30 and 40 km, while the projection in Figure 5(d) indicates a value hovering around unity from 40 to 50 km. Figure 5(d) is identical to Figure 3 in the main text.

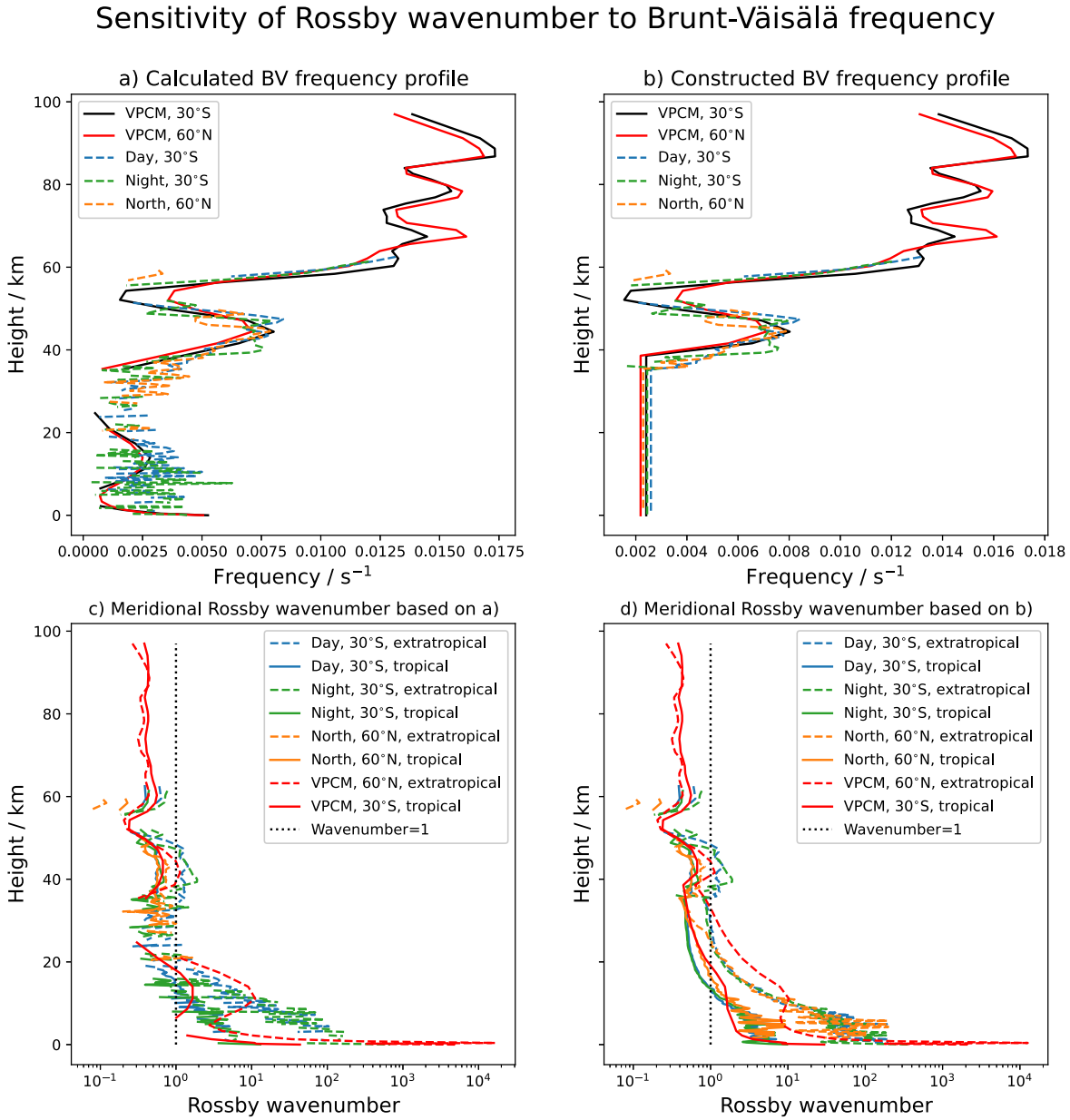

Figure 5. Top row: (a) Brunt–Väisälä frequency calculated as $N = \sqrt{\frac{g}{\theta(z)}\frac{d\theta}{dz}}$ and (b) Brunt–Väisälä frequency with values below 40 km replaced by the mean for this region (approximately 0.0025 s^{-1}). Values above 40 km are the same as in (a). Bottom row: tropical and extratropical meridional Rossby wavenumbers calculated according to Equations (1) and (2) using each of the Brunt–Väisälä frequency profiles shown in the row above. Subfigure (d) is used in the main text to diagnose the circulation regimes.

A.2. Sensitivity to Latitude

In Figure 6, we show the effect of using wind and temperature profiles from different latitudes of the VPCM simulation on the tropical and extratropical meridional Rossby wavenumbers. Figure 6(a) shows that all latitudes equatorward of 60° give a very similar result for the tropical Rossby radius, with the tropical wavenumber equal to one at 20 km. Figure 6(b) shows that latitudes from 30° to 75° give similar results and are a good fit to the circulation regime change, while the profiles at the equator and near the pole, where the sine function becomes 0, are outliers. As it is debatable which latitude best represents a global-scale phenomenon, we use latitude values in Figure 3 to match the entry latitudes of the Pioneer Venus probes.

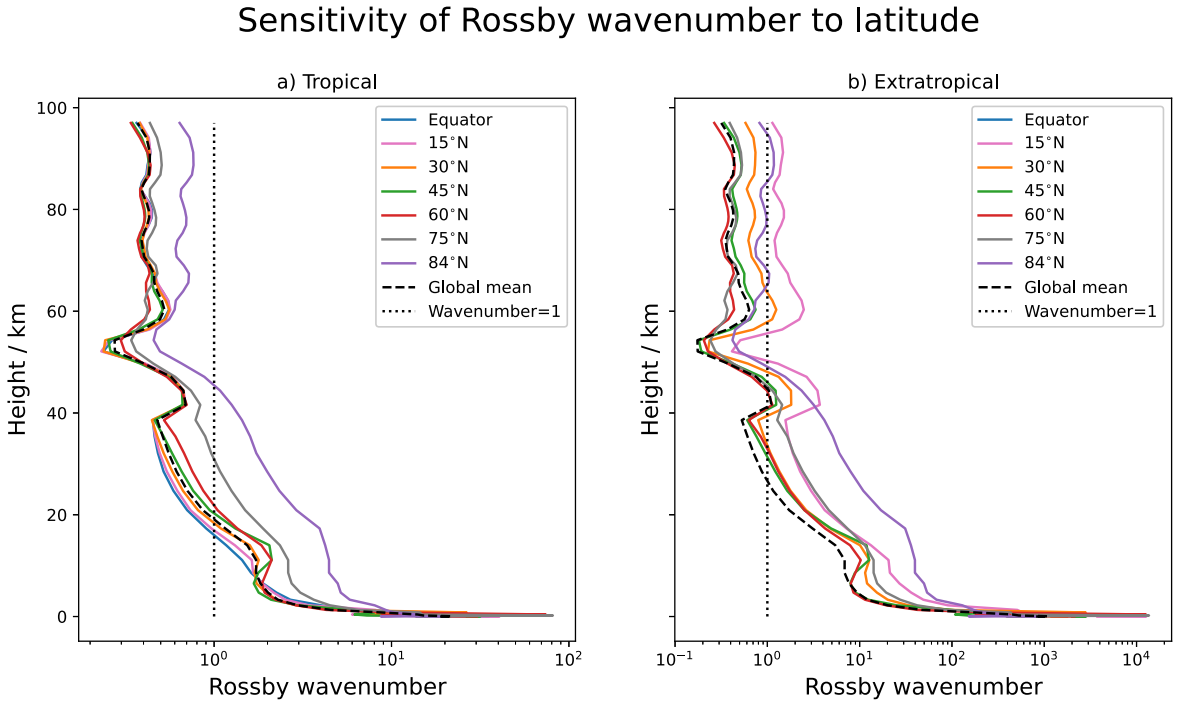

Figure 6. Tropical and extratropical meridional Rossby wavenumbers calculated according to Equations (1) and (2) using wind profiles from a range of latitudes, as well as the area-weighted global mean.

A.3. Animations

We include animations of Figures 1 and 4(a) to show how the circulation and waves develop over time. Both animations are created from the *Surface* dataset linked in Section Data Availability and cover 3 Venus days with a frame/output frequency of 20 frames per Venus day. This means they capture the 36 day wave and solar tides, but neglect the 4–5 day waves. In the animated Figure 1(d) (42 km altitude), the 36 day wave structure is easy to see as there are no other prominent competing waves. In Figure 1(f) (64 km altitude), the 36 day wave can be seen moving at the high latitudes in sync with the deeper model level (42 km), but sometimes other waves become more prominent: an equatorial wave and (occasionally) a high-latitude tidal gyre (period of 1 solar day). In the animated Figure 4, the 36 day wave is the tilted antisymmetric structure seen below 70 km. Above this is a stronger wave with a period of 1 solar day (the high-latitude tidal gyre).

ORCID iDs

Maureen Cohen https://orcid.org/0000-0001-5014-4174
James Holmes https://orcid.org/0000-0003-3018-2135
Stephen Lewis https://orcid.org/0000-0001-7237-6494
Manish Patel https://orcid.org/0000-0002-8223-3566
Sébastien Lebonnois https://orcid.org/0000-0002-2390-8164

References

Armstrong, D. J., de Mooij, E., Barstow, J., et al. 2016, NatAs, 1, 0004
Asnodkar, A. P., Wang, J., Eastman, J. D., et al. 2022, AJ, 163, 155
Barnes, R. 2017, CeMDA, 129, 509
Belton, M. J. S., Smith, G. R., Schubert, G., & Genio, A. D. D. 1976, JAtS, 33, 1394
Carone, L., Keppens, R., & Decin, L. 2015, MNRAS, 453, 2412
Cohen, M., Bollasina, M. A., Sergeev, D. E., Palmer, P. I., & Mayne, N. J. 2023, PSJ, 4, 68
Cohen, M., Holmes, J., Lewis, S., & Patel, M. 2024, PSJ, 5, 219
Collard, A. D., Taylor, F. W., Calcutt, S. B., et al. 1993, P&SS, 41, 487
Counselman, C. C., Gourevitch, S. A., King, R. W., Loriot, G. B., & Ginsberg, E. S. 1980, JGRA, 85, 8026
Counselman, C. C., Gourevitch, S. A., King, R. W., Loriot, G. B., & Prinn, R. G. 1979, Sci, 205, 85
Covey, C., & Schubert, G. 1982, JAtS, 39, 2397
Dawson, A. 2016, JORS, 4, e31
Debras, F., Mayne, N., Baraffe, I., et al. 2020, A&A, 633, A2
Deming, L. D., & Seager, S. 2017, JGRE, 122, 53
Dutton, J. 1976, The Ceaseless Wind: An Introduction to the Theory of Atmospheric Motion (New York: McGraw-Hill)
Edson, A., Lee, S., Bannon, P., Kasting, J. F., & Pollard, D. 2011, Icar, 212, 1
Eymet, V., Fournier, R., Dufresne, J.-L., et al. 2009, JGRE, 114, E11008
Fauchez, T. J., Turbet, M., Wolf, E. T., et al. 2020, GMD, 13, 707
Garate-Lopez, I., & Lebonnois, S. 2018, Icar, 314, 1
Genio, A. D. D., & Rossow, W. B. 1990, JAtS, 47, 293
Gierasch, P. J. 1975, JAtS, 32, 1038
Hammond, M., & Lewis, N. T. 2021, PNAS, 118, 13
Hammond, M., & Pierrehumbert, R. T. 2018, ApJ, 869, 65
Hammond, M., Tsai, S.-M., & Pierrehumbert, R. T. 2020, ApJ, 901, 78
Haqq-Misra, J., Wolf, E. T., Fauchez, T. J., Shields, A. L., & Kopparapu, R. K. 2022, PSJ, 3, 260
Haus, R., Kappel, D., & Arnold, G. 2015, P&SS, 117, 262
Hochman, A., Luca, P. D., & Komacek, T. D. 2022, ApJ, 938, 114
Holton, J. R., & Hakim, G. H. 2013, An Introduction to Dynamic Meteorology (5th edn.; Oxford: Academic Press)
Horinouchi, T., Hayashi, Y.-Y., Watanabe, S., et al. 2020, Sci, 368, 405
Horinouchi, T., Satoh, T., & Peralta, J. 2023, GeoRL, 50, e2022GL101633
Hou, A. Y., & Farrell, B. F. 1987, JAtS, 44, 1049
Hourdin, F., Couvreux, F., & Menut, L. 2002, JAtS, 59, 1105
Hourdin, F., Musat, I., Bony, S., et al. 2006, ClDy, 27, 787
Hourdin, F., Van, P. L., Forget, F., & Talagrand, O. 1993, JAtS, 50, 3625
Imai, M., Takahashi, Y., Watanabe, M., et al. 2016, Icar, 278, 204
Imamura, T., Mitchell, J., Lebonnois, S., et al. 2020, SSRv, 216, 87
Karyu, H., Kuroda, T., Itoh, K., et al. 2023, JGRE, 128, e2022JE007595
Khatuntsev, I. V., Patsaeva, M. V., Titov, D. V., et al. 2013, Icar, 226, 140
Knutson, H. A., Charbonneau, D., Cowan, N. B., et al. 2008, ApJ, 690, 822
Komacek, T. D., & Abbot, D. S. 2019, ApJ, 871, 245
Kouyama, T., Imamura, T., Nakamura, M., Satoh, T., & Futaana, Y. 2012, P&SS, 60, 207
Lai, D., Lebonnois, S., & Li, T. 2024, JGRE, 129, e2023JE008253

Landgren, E., Nadeau, A., Lewis, N., Kataria, T., & Hitchcock, P. 2023, PSJ, 4, 106
Lebonnois, S., Hourdin, F., Eymet, V., et al. 2010, JGRE, 115, E06006
Lebonnois, S., Sugimoto, N., & Gilli, G. 2016, Icar, 278, 38
Leconte, J., Forget, F., Charnay, B., et al. 2013, A&A, 554, A69
Lee, C., Lewis, S. R., & Read, P. L. 2007, JGRE, 112, E04S11
Marcq, E., Bzard, B., Encrenaz, T., & Birlan, M. 2005, Icar, 179, 375
Marcq, E., Encrenaz, T., Bzard, B., & Birlan, M. 2006, P&SS, 54, 1360
Mayne, N. J., Baraffe, I., Acreman, D. M., et al. 2014, A&A, 561, A1
Merlis, T. M., & Schneider, T. 2010, JAMES, 2, 13
Mitchell, J. L., & Vallis, G. K. 2010, JGRE, 115, E12008
Newman, M., Schubert, G., Kliore, A. J., & Patel, I. R. 1984, JAtS, 41, 1901
Noda, S., Ishiwatari, M., Nakajima, K., et al. 2017, Icar, 282, 1
Penn, J., & Vallis, G. K. 2018, ApJ, 868, 147
Pierrehumbert, R. T., & Hammond, M. 2019, AnRFM, 51, 275
Plumb, R. A. 1975, QJRMS, 101, 763
Rossow, W. B., Genio, A. D. D., & Eichler, T. 1990, JAtS, 47, 2053
Rossow, W. B., & Williams, G. P. 1979, JAtS, 36, 377
Sánchez-Lavega, A., Lebonnois, S., Imamura, T., Read, P., & Luz, D. 2017, SSRv, 212, 1541
Seiff, A., Kirk, D. B., Young, R. E., et al. 1980, JGRA, 85, 7903
Seiff, A., Schofield, J. T., Kliore, A. J., et al. 1985, AdSpR, 5, 3
Sergeev, D. E., Lewis, N. T., Lambert, F. H., et al. 2022, PSJ, 3, 214
Showman, A., Cho, J., & Menou, K. 2010, Exoplanets, Space Science (Tucson, Arizona: Univ. Arizona Press), 471
Showman, A. P., & Polvani, L. M. 2011, ApJ, 738, 71
Showman, A. P., Wordsworth, R. D., Merlis, T. M., & Kaspi, Y. 2013, in Comparative Climatology of Terrestrial Planets, ed. S. J. Mackwell et al. (Tucson, AZ: Univ.of Arizona Press), 277
Skinner, J. W., & Cho, J. Y.-K. 2022, MNRAS, 511, 3584
Sugimoto, N., Takagi, M., & Matsuda, Y. 2014a, JGRE, 119, 1950
Sugimoto, N., Takagi, M., & Matsuda, Y. 2014b, GeoRL, 41, 7461
Suzuki, A., Takagi, M., Ando, H., et al. 2022, JGRE, 127, e2022JE007243
Takagi, M., Ando, H., Imai, M., Sugimoto, N., & Matsuda, Y. 2023, JGRE, 128, e2023JE007922
Takagi, M., Ando, H., Sugimoto, N., & Matsuda, Y. 2022, JGRE, 127, e2021JE007164
Takagi, M., & Matsuda, Y. 2007, JGRD, 112, D09112
Takagi, M., Sugimoto, N., Ando, H., & Matsuda, Y. 2018, JGRE, 123, 335
Tan, X., & Komacek, T. D. 2019, ApJ, 886, 26
Tsai, S.-M., Dobbs-Dixon, I., & Gu, P.-G. 2014, ApJ, 793, 141
Tsang, C. C. C., & McGouldrick, K. 2017, Icar, 289, 173
Tsang, C. C. C., Taylor, F. W., Wilson, C. F., et al. 2009, Icar, 201, 432
Yamamoto, M., Hirose, T., Ikeda, K., Takahashi, M., & Satoh, M. 2023, Icar, 392, 115392
Yamamoto, M., Ikeda, K., Takahashi, M., & Satoh, M. 2024, Icar, 411, 115921
Yamamoto, M., & Takahashi, M. 2003, JAS, 60, 561
Yamamoto, M., & Takahashi, M. 2004, GeoRL, 31, L09701
Yamamoto, M., & Takahashi, M. 2006, JAtS, 63, 3296